Multi-modal Framework for Automatic Detection of Diagnostically Important Regions in Nonalcoholic Fatty Liver Ultrasonic Images

Abstract

The severity of fat in ultrasonic liver images is quantified based on characteristics of three regions in the image namely diaphragm, periportal veins and texture of liver parenchyma. The characteristics of these regions vary with the severity of fat in the liver, and is subjected to low signal to noise ratio, low contrast, poorly defined organ boundaries, etc., hence locating these regions in ultrasound images is challenging task for the sonographers. Automated detection of these regions will help the sonographers to do accurate diagnosis in shorter time, and also acts as a fundamental step to develop automated diagnostic algorithms. In this paper, we propose a novel multi-modal framework for detecting diaphragm, periportal veins and texture of liver parenchyma in ultrasonic liver ultrasound images. Since the characteristics of these regions differ from each other, we propose a specific algorithm for detecting each region. Diaphragm and periportal veins are detected with the combination of Viola Jones and GIST descriptor based classifier, while homogeneous texture regions are detected with the combination of histogram features based classifier and connected components algorithm. The proposed algorithm when tested on 180 ultrasound liver images, detected the diaphragm, periportal veins and texture regions with an accuracy of 97%, 91% and 100% respectively.

Keywords: Steatosis, Diaphragm, Periportal veins, Ultrasonic liver parenchyma texture, Viola Jones, GIST, Histogram features.

1. Introduction

Nonalcoholic Fatty Liver Disease (NAFLD) is one of the leading cause for the dysfunction of the liver and prevalent in 30% of general population in the developed countries [1]. If NAFLD is untreated, it may progress into chronic liver diseases such as fibrosis, cirrhosis, hepatocellular carcinoma, liver cancer, etc [2], [3]. Depending on the severity of fat, the liver is categorized into Normal, Grade I, Grade II and Grade III respectively. If the density of fat is less than 5% it is considered as Normal, 5 to 33% as Grade I, 33 to 66% as Grade II and greater than 66% as Grade III respectively [4]. The severity of fat in the liver is determined using invasive and noninvasive procedures. Invasive procedures which include blood tests and biopsies are associated with complications like bleeding, bile leakage and infections. Hence doctors recommend for noninvasive procedures like Magnetic Resonance Imaging (MRI), Computed Tomography (CT) and ultrasound scanning [5, 6]. MRI and CT being expensive, doctors prefer for ultrasound scanning which has the advantages of real-time imaging, safety and less expensive [7, 8]. Although the ultrasound scanning is widely used, the diagnostic accuracy in quantifying the fat in the liver is very low due to the subjectivity involved in the scanning. Strauss et al. found that there is a low mean inter and intra-observability of 72% and 76% respectively in discriminating between normal and fatty liver, while inter and intra-observability of 47-59% and 59-64% respectively is observed in discriminating the severity of fat within Grade I, Grade II and Grade III classes. It is also found that 32 to 34% of fatty liver images belong to Grade I and Grade II are not distinguishable to sonographers eye [9]. Therefore there is a need for computer-aided diagnosis (CAD) algorithms to assist the sonographers to accurately diagnose the fatty liver diseases.

In literature [6, 10, 11, 12, 13, 14, 15, 16, 17, 18, 19], authors are mainly focused on developing CAD algorithms for discriminating normal liver with fatty liver images, where fatty liver constituted liver images ranging from Grade I to Grade III category, while further distinction within the fatty liver grades is not extensively studied [20]. Accurate quantification of fat in the liver carries paramount importance in liver diagnosis, for example in liver transplantation, even a Grade I fatty liver of donor can increase the potentiality of liver failure in the recipient and also there is a high probability that the donor will get diseased [6, 21]. The patients who undergo liver resections with Grade III fatty liver are expected likely to suffer from post-operative complications [22]. Therefore accurate quantification of fat in the liver will prevent the patients to suffer from chronic diseases and complications associated with NAFLD. In [20, 23, 24, 25, 26, 27, 28], the authors proposed CAD algorithms for quantifying the fatty content in the liver. In all these algorithms, authors employed manual cropping for detecting the region of interest (RoI). RoI includes the homogeneous texture of liver parenchyma, pixels along the direction of wave propagation, etc. To avoid manual intervention in CAD, researchers proposed algorithms which works on complete images [17, 29, 30, 31, 32]. While dealing with entire image, we are extracting the features from the regions which is neither important nor convey information useful for diagnosis leading to ineffective feature representation. Hence, in developing CAD algorithms, we have to ensure that the features are extracted only from diagnostically important regions. Detecting RoI's in ultrasonic liver images is challenging due to

- Low signal to noise ratio, poorly defined organ boundaries, low contrast, artifacts caused due to acoustic shadows, etc.
- Variation in the characteristics of the RoI within intraclass and interclass images.

In this paper, we propose an algorithm for automated detection of the RoI's useful for quantifying the fat in liver ultrasound images. The quantification of fat in the liver through ultrasound scanning is done by perceiving characteristics in three regions of the liver such as diaphragm, periportal veins and texture of liver parenchyma. The RoI's of the diaphragm, periportal veins and texture of liver parenchyma of the liver ultrasound image is shown in Fig. 1. The characteristics of these region vary accordingly with the severity of fat present

Table 1: Characteristics of the diaphragm, periportal veins and texture of liver parenchyma corresponding to different grades of fatty liver [20], [33].

Category	**Characteristics**
Normal	Visible echogenicity with visible periportal and diaphragm. The texture of liver parenchyma appears coarser and rugged.
Grade I	Increased hepatic echogenicity with visible periportal and diaphragmatic echogenicity. The texture appears less coarser and smooth.
Grade II	Increased hepatic echogenicity with imperceptible periportal echogenicity with partial obscuration of diaphragm. The texture appears more smooth and finer.
Grade III	Increased hepatic echogenicity with imperceptible periportal echogenicity and obscuration of diaphragm. The texture appears diffused and appears more finer.

in the liver. The characteristics of these RoI's with respect to different grades of fatty liver is discussed in Table. 1 [20], [33]. Based on the characteristics of RoI's, the sonographers quantify the fat in the liver. Automatic detection of these regions will assist sonographers to make an accurate diagnosis in short time and also serves as a fundamental step for the development of robust automated diagnostic algorithms for quantification of fat in the liver.

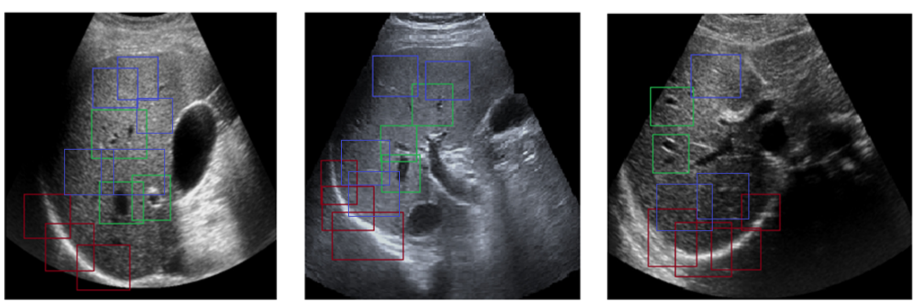

Figure 1: Ultrasonic liver images. Red boxes indicates the diaphragm, green boxes indicates periportal veins and blue boxes indicates RoI corresponding to homogeneous texture.

In this paper, we propose an automatic algorithm for detection of diaphragm, periportal veins and homogeneous texture regions of liver parenchyma. Since each RoI is different with respect to other RoI's, we developed a specific algorithm for detecting each RoI. The novelties of the paper are:

- For detecting RoI of a diaphragm, we propose an algorithm which is a combination of Viola Jones (VJ) algorithm [34], GIST descriptor [35] based cubic SVM classifier and active contour segmentation [36, 37]. The VJ algorithm and GIST descriptor based classifier is trained appropriately with the images corresponding to the regions of the diaphragm.

- For detecting RoI of periportal veins, we propose an algorithm which is a combination of VJ and GIST descriptor based quadratic SVM classifier. Each classifier is trained appropriately with the images corresponding to the regions of periportal veins.

- For detecting RoI for the texture of liver parenchyma, we propose a two-stage classifier framework, which is based on the combination of histogram features based Gausssian SVM classifier and connected components algorithm [38]. The histogram based quadratic SVM classifier is trained with the images of homogeneous and nonhomogeneous regions of liver parenchyma.

All the three algorithms are applied independently on the image to detect RoI's of the ultrasonic liver image. The main contributions of our work lie in developing and integrating different classification frameworks to detect all the RoI's. The performance of the proposed algorithm is evaluated based on its individual accuracy in detecting each RoI. The detail explanation regarding the detection of each RoI is discussed in Section 2.

The rest of the paper is organized in the following way. In Section 2, we discuss in detail about the proposed framework for detecting multiple RoI's. In Section 3, we discuss the database used, and the protocols followed in image acquisition. Results of the proposed algorithm is reported in Section 4, and Section 5 concludes the paper with implications and future scope of the work.

2. Multi-modal framework for automatic detection of the diaphragm, periportal veins and homogeneous texture of liver parenchyma.

The block diagram representation of the proposed algorithm is shown in Fig. 2. The framework consists of three independent algorithms each specifically proposed for detecting RoI of a diaphragm, periportal veins and texture of liver parenchyma. The detailed description regarding the detection of each RoI is discussed in the following sections.

2.1. Diaphragm detection

The diaphragm appears like a slanted 'U' shape with an upper part trimmed in the liver ultrasound image. The shape, size and length of a diaphragm depends on the anatomy of patient and position of the probe used to acquire the liver images. Since the diaphragm lies above the liver, it appears in a lower left portion of the ultrasound image when captured from a subxiphoid view [39]. The block diagram representation of the proposed algorithm for detecting RoI of a diaphragm is shown in Fig. 3. Initially, VJ algorithm is used to detect the RoI of a diaphragm. VJ algorithm which is primarily proposed for detecting faces in real-time also proved that the same framework is effective in detecting other parts like noses, eyes, upper body parts, cars, stop signs, etc. Recently VJ algorithm has been used in medical image analysis to detect organs like carotid artery, kidney, pelvis and proximal femur of a hip joint, etc [40, 41, 42], [43]. The VJ algorithm works in three stages namely feature extraction, AdaBoost training and cascade of classifiers.

2.1.1. Feature extraction

In this stage, Haar-like features are extracted from the positive and negative training images. Haar features are extracted using two, three, and four rectangular kernels [44], resulting in large number of features. For an image of size 24×24 a total of 45,396 features were extracted. For computing these

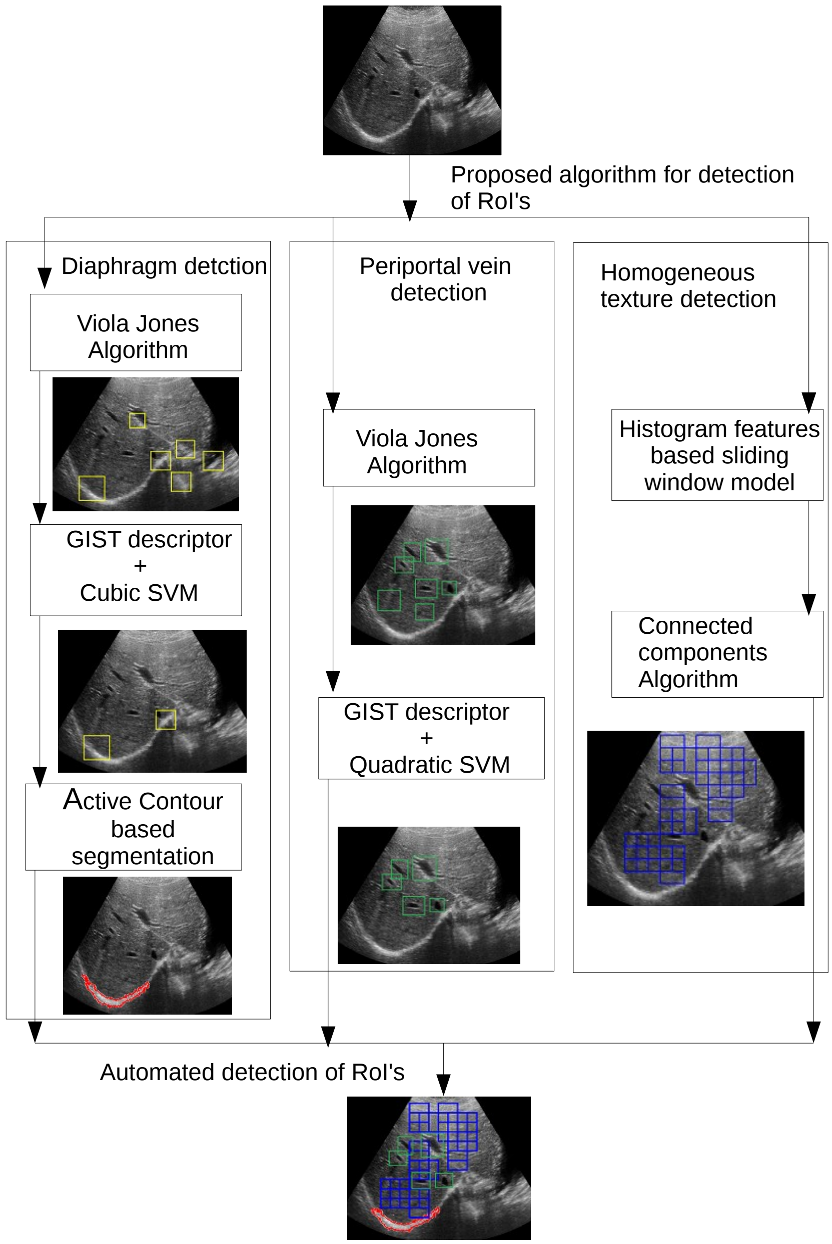

Figure 2: Block diagram representation of the proposed algorithm for detection of RoI's in the liver ultrasound image.

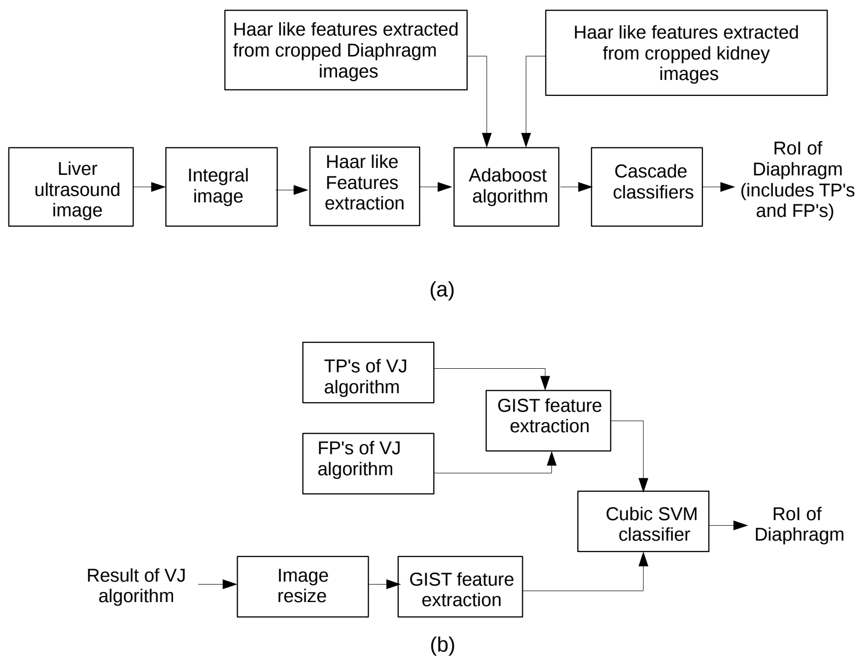

Figure 3: (a). Block diagram representation of the VJ algorithm used for detecting the RoI of a diaphragm and (b). Algorithm used to reduce the FP's resulted from VJ algorithm.

many number of features with less computational complexity, an intermediate image representation called integral image approach is employed [45]. To make the RoI detection scale invariant, the features are extracted on a pyramid of 11 images where each image is 1.25 times greater than the previous image.

2.1.2. AdaBoost based feature selection and learning algorithm

All the extracted features from RoI are not useful for classification, and training a classifier with these many number of features is a computationally expensive procedure. To find the most representative features to train a classifier, an AdaBoost algorithm is used [46]. The decision stumps are used as weak learners for classification. The AdaBoost algorithm improves the classification performance by combining a collection of weak learners.

2.1.3. Cascade classifier

To improve the detection accuracy and to reduce the computation time, a cascade of classifiers is used. Each cascade classifier is trained with a combination of weak learners. The complexity of detecting the RoI increases with increase in the number of cascaded classifiers. The cascaded classifier architecture improves the detection rate by eliminating the diaphragms in earlier stages of the cascaded classifiers. The negative and positive images used in training the VJ algorithm for detecting RoI of a diaphragm is shown in Fig. 4 and Fig. 5. The positive images are extracted by cropping diaphragm from liver ultrasound images. The size of diaphragm used in training the VJ algorithm is varied in the range 48×48 to 64×78 pixels. The entire region of the diaphragm is not considered for training due to the complex and varied structure of the diaphragm. While for negative training images, care is taken that the images do not contain shapes resembling like a diaphragm. We choose kidney ultrasound images as negative training examples since no part of the kidney image resemble like a diaphragm. The VJ algorithm is trained with 741 labeled diaphragms and 50 kidney images. The RoI's detected by the VJ algorithm is shown in Fig. 6. Although VJ algorithm results with high accuracy in detecting the diaphragm,

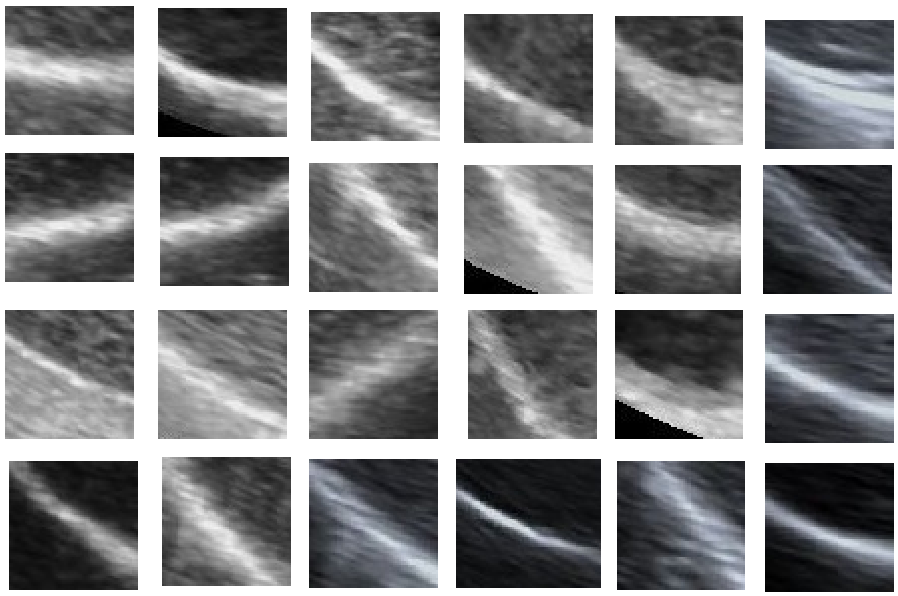

Figure 4: Images used as positive examples in training the VJ algorithm for detection of diaphragm.

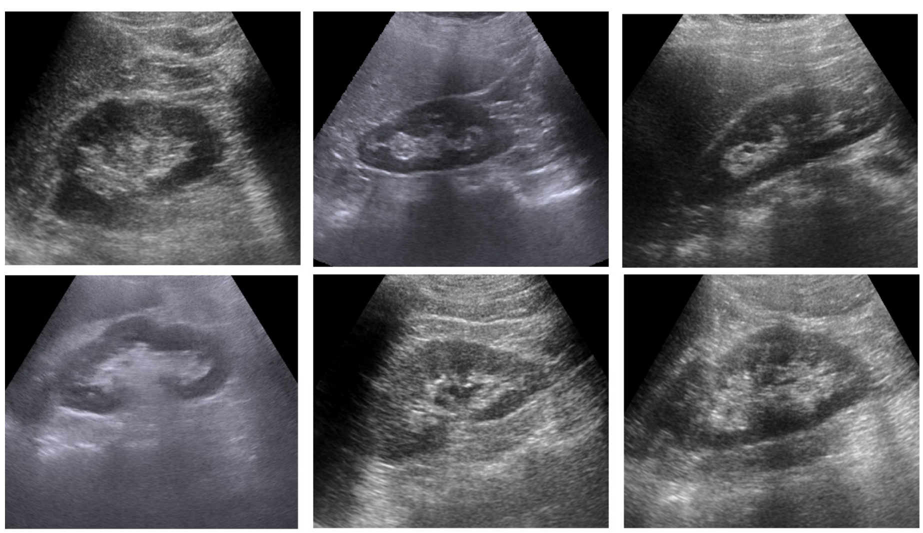

Figure 5: Images used as negative examples in training the VJ algorithm for detection of diaphragm. All these images belongs to the kidney.

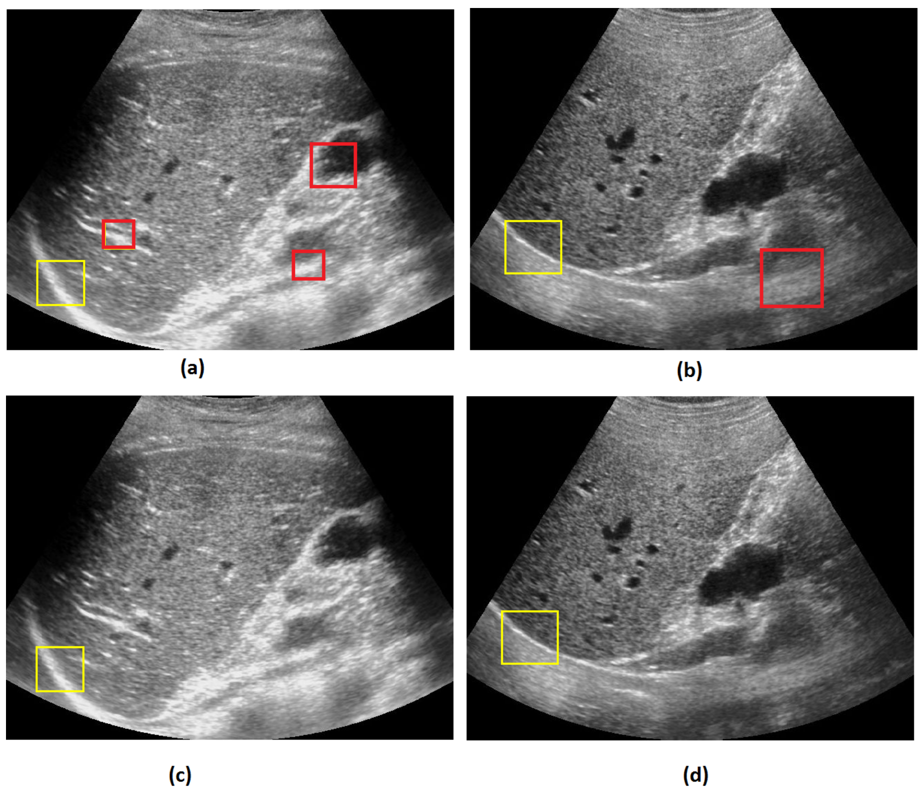

Figure 6: The red rectangular boxes indicates the FP's and the yellow rectangular boxes indicates the true positives. (a), (b) Result of the VJ algorithm in detecting the diaphragm. (c), (d) Elimination of the FP's after applying GIST based cubic SVM classification.

it suffered from high false positives (FP's). While developing CAD algorithms, care should be taken that the algorithm will result in less number of FP's, since analyzing the FP's for diagnosis will lead to a faulty diagnosis. The VJ algorithm mostly detected border of vein walls and nonhomogeneous texture regions as FP's. To eliminate FP's, a supervised learning algorithm trained with true positives (TP's) and FP's resulted from the VJ algorithm is developed. The intuition of considering TP's and FP's of VJ is to make the classifier robust to the false detections. The algorithm is tested with some of the popularly used texture features like Histogram of Oriented Gradients (HOG) [47], histogram and GIST descriptor [35]. Out of all these features, GIST descriptor performed better in eliminating the FP's.

2.1.4. GIST descriptor based SVM classifier

The block diagram representation regarding the classification between TP's and FP's is shown in Fig. 3b. The TP's and FP's resulted from VJ algorithm is of different size. Hence in developing the algorithm, all the TP's and FP's images are resized to a fixed resolution of 64×64 pixels, this size is chosen based on the cross-validation. From each resized image, GIST descriptor is extracted. GIST descriptor gives the low dimensional representation of the scene by extracting the spatial envelope of an image [48]. GIST represent the features like naturalness, ruggedness, openness, roughness and expansion of a scene [49]. GIST descriptor from image is extracted in the following way. Initially, the image is convolved with 32 Gabor filters corresponding to four scales and eight orientation resulting in 32 feature maps. Each feature map is divided into 4×4 grid resulting in 16 regions. The coefficients of each region is averaged resulting in 16 features for each feature map. The averaged values of all 32 feature maps will result in a total of $16\times32=512$ GIST descriptor. The extracted features are then used to train the cubic SVM classifier. The classifier is trained with 250 TP's and 896 FP's images resulted from the VJ algorithm. With 5 fold cross-validation scheme, the algorithm resulted with an accuracy of 94.6% in classifying TP's and FP's.

After applying the GIST descriptor based SVM classification, the FP's have been significantly reduced. But the output of these algorithm will not give the complete detection of the diaphragm. For complete detection of the diaphragm, active contour-based segmentation [36], active shape modeling (ASM) [50] algorithms can be is used. ASM model fails due to high nonrigidness in the shape of the diaphragm. Hence we employed active contour-based segmentation for detecting the entire contour of a diaphragm.

2.1.5. Active contour based segmentation

The block diagram representation for the active contour-based segmentation is shown in the Fig. 7. Segmenting RoI in ultrasound image poses a lot of difficulties due to large variations observed in the diaphragm from image to image. The Active Contour Model (ACM)[36] helps to obtain closed object contour as a segmentation result under the circumstances of noise and poorly defined boundaries. Many variants of active contours like gradient vector flow [51], balloon model [52], diffusion snakes [53], active contours with edges [36], geodesic active contours [54], etc., have been proposed in the literature for effective segmentation. In this paper, we employed region-based active contour segmentation [36] to segment the diaphragm region. Active contour is an iterative process, which detects the contour based on the evolution. For segmenting the image, we need to set the initial state of the active contour by initializing the mask near to the diaphragm. The output obtained after VJ and GIST feature based cubic SVM classifier is used as a mask for initializing the active contour. Curve evolution is stopped when there is no further displacement in the curve, or it can be stopped forcibly by fixing the number of iterations. In this work, 300 iterations is needed for complete detection of the diaphragm. The performance of the segmentation task is not quantified in this paper since the focus of the work is laid in detecting the RoI for the diaphragm which is used for developing CAD algorithms. The performance of the active contour-based segmentation for diaphragm detection is shown in Fig. 8.

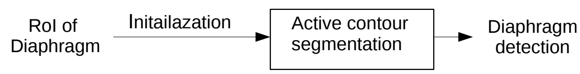

Figure 7: Block diagram representation for the active contour model based segmentation of a diaphragm.

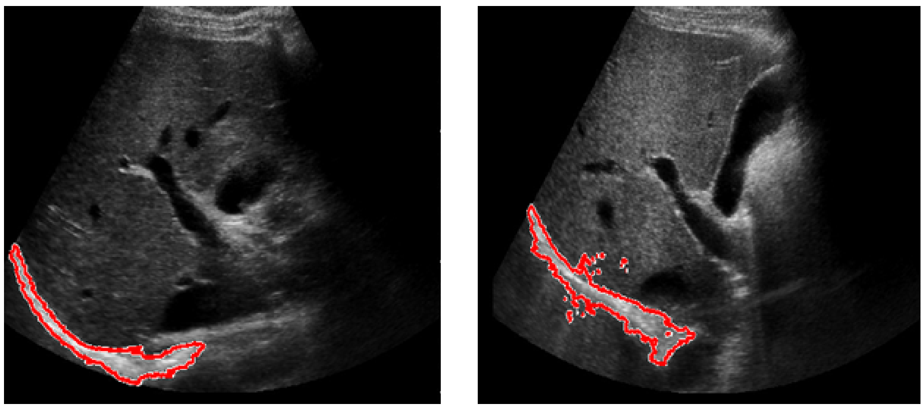

Figure 8: Diaphragm detection based on active contour segmentation after 300 iterations.

2.2. Periportal vein detection

The algorithm which is used to detect RoI for diaphragm also worked effectively in detecting the periportal veins. The segmentation algorithm is not employed for periportal vein detection since the entire vein is enclosed inside the RoI. Periportal veins are detected in two stages, in the initial stage, VJ algorithm is used to detect the periportal veins. The positive training images used to train the VJ algorithm is shown in Fig. 9. In general, more than one periportal vein vessels will appear in liver ultrasonic images, hence all the visible periportal veins are considered in training the VJ algorithm. The size of cropped images employed in training the VJ algorithm are in the range of 15 $\times$ 25 to 32 $\times$ 42 pixels. The positive training images are extracted by cropping the periportal veins corresponding to all grades of fatty liver. We used the same negative training images (refer Fig. 5,) which we have used for training the

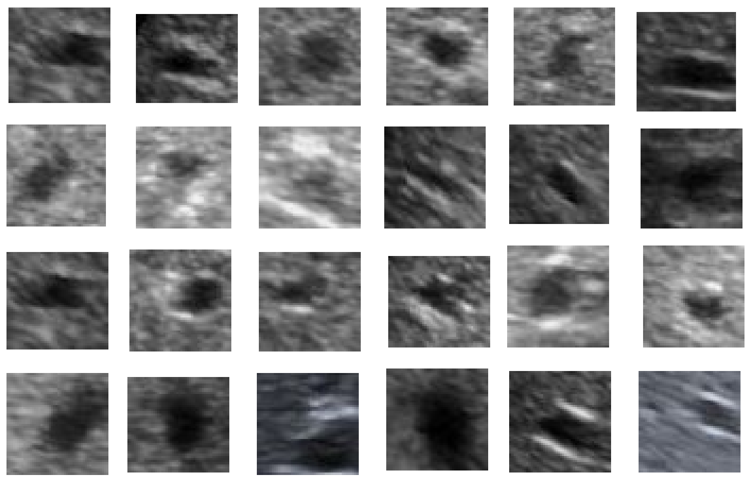

Figure 9: Images used in training the VJ algorithm for detecting the periportal veins.

VJ algorithm for detecting the diaphragm detection. Care is taken that kidney images used in negative training examples do not have cyst abnormalities, since the cyst in kidney resembles like a periportal vein in the liver ultrasound image. The VJ algorithm is trained with 829 labeled periportal veins and 50 kidney images. The VJ algorithm has resulted in both TP's and FP's as shown in Fig. 10. The regions where there is enough contrast in images are detected as FP's, since the periportal veins also provide similar contrast in their respective spatial locations. To eliminate the FP's, a second stage classifier algorithm with GIST descriptor and quadratic SVM classifier is employed. The second stage classifier algorithm is trained with TP's and FP's of the VJ algorithm which is developed for detecting the periportal veins. Before training the classifier, the sizes of all TP's and FP's are resized to a standard 32×32 pixel size, this size is chosen based on cross validation. The second stage of the classification algorithm is trained with 350 images of TP's and 200 images of FP's resulted from the VJ algorithm. With 5 fold cross-validation, the GIST descriptor based quadratic SVM classifier resulted in an accuracy of 93.7% in classifying TP's and FP's of periportal veins.

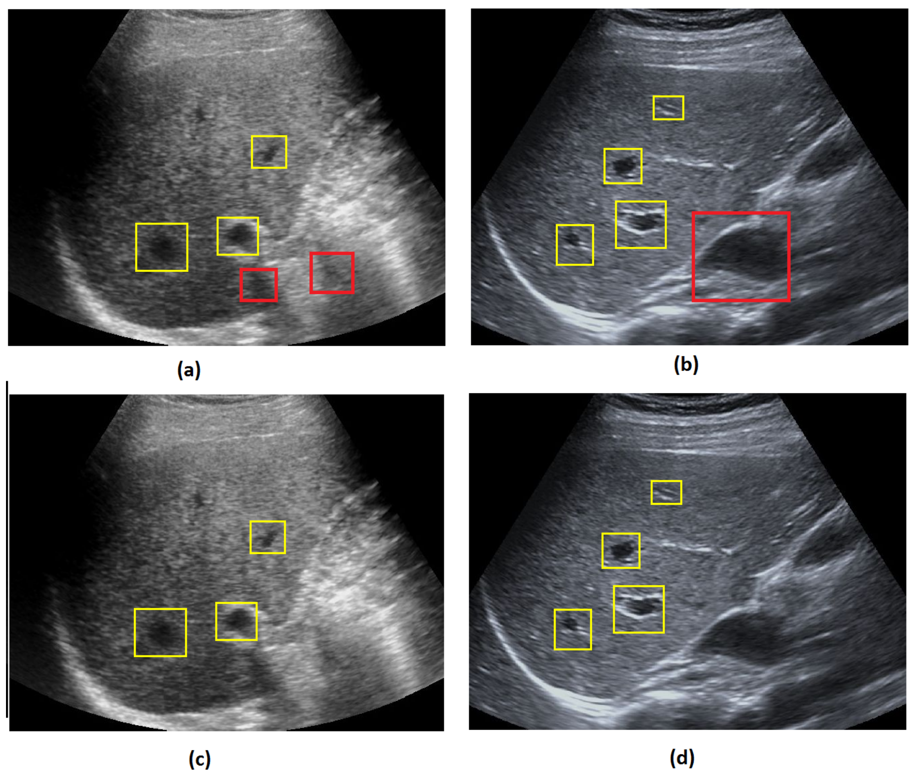

Figure 10: Automated periportal vein detection. Red boxes indicates the FP's and yellow boxes indicates TP's. (a), (b) Performance of the VJ algorithm in detecting the periportal veins. (c), (d) Performance of the algorithm after applying the GIST feature based quadratic SVM classifier.

2.3. Homogeneous texture detection

The block diagram representation regarding the detection of RoI for homogeneous textures in liver parenchyma is shown in Fig. 11. Since the texture does not have any shape specific information, the VJ algorithm performed poorly in detecting the RoI in a liver. The liver mainly consists of periportal veins, the texture of liver parenchyma and diaphragm. Therefore, the RoI detection for homogeneous texture is framed as a binary classification problem, where one class belongs to RoI of homogeneous texture regions and another class belongs to RoI's of the diaphragm and periportal veins. The homogeneous texture is better represented with histogram features; these include mean, variance, skewness and kurtosis. The histogram appeared symmetry for homogeneous texture and nonsymmetry for nonhomogeneous texture regions giving discriminative representation across the homogeneous and nonhomogeneous RoI's. The homogeneous RoI's in liver parenchyma is detected using a sliding window based approach. A window of size 64×64 with the sliding length of 32 pixels is chosen for the analysis. The Gaussian SVM classifier is used to discriminate homogeneous and nonhomogeneous regions based on the histogram features. The homogeneous texture patches used in training the classifier is shown in Fig. 12. A total of 400 homogeneous textures and 550 diaphragm and periportal images extracted from all grades of fatty liver is used in training the Gaussian SVM classifier. The sliding window model resulted with 100% accuracy in detecting the homogeneous texture regions along with the FP's. The FP's are resulted due to periportal veins. Since the periportal veins appears as blobs, we eliminated the FP's by detecting the blobs in the homogeneous region. This is done by using a connected components algorithm [38]. The connected components algorithm is applied in the following way. Initially each detected homogeneous texture is binarized by setting a threshold to 20. The value 20 is chosen based on the cross validation. The pixels with intensity value less than 20 is set to '0', while the pixels with intensity greater than or equal to threshold 20 is set to '1'. Then the number of pixels in each blob is computed by fixing a connectivity to 6. It is found that we can eliminate all FP's present in the liver parenchyma

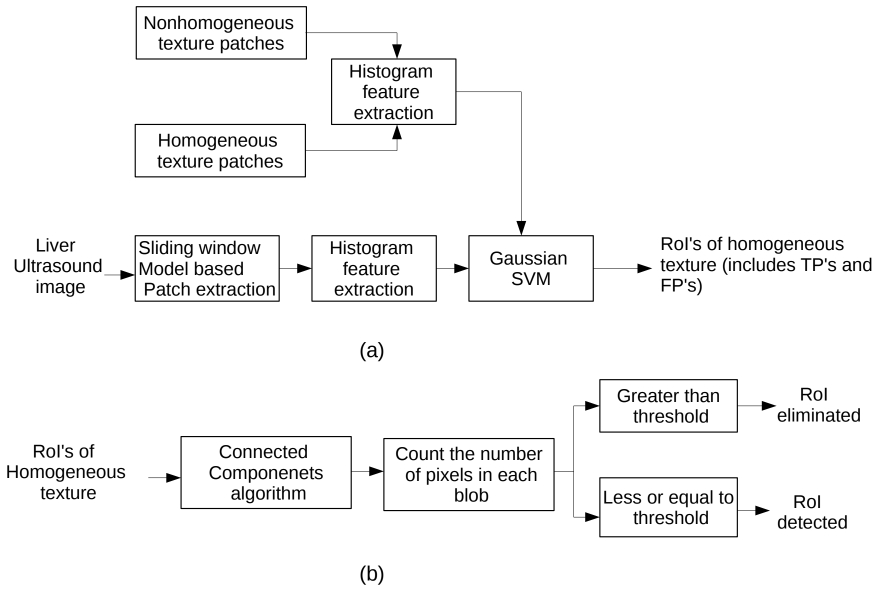

Figure 11: Algorithm for detecting RoI corresponding to homogeneous texture of liver parenchyma.

whose pixel count in each blob is more than 15. The optimal values for the connected components algorithm is chosen based on the experimental analysis. The performance of the proposed algorithm in detecting the homogeneous textures is shown in Fig. 13. The multiple RoI's are obtained for the homogeneous texture since the parenchyma covers wide area in the liver.

2.4. SVM classifier

SVM is a binary classifier, which learns a model that best separates the features of two classes [55]. SVM can only work if the features of the classes are linearly separable. To work with linearly non-separable data, SVM is operated with various kernel functions [56]. The kernel function projects the features into higher dimensions where the data becomes linearly separable. In this work, we evaluated the performance of the SVM classifier with respect to linear,

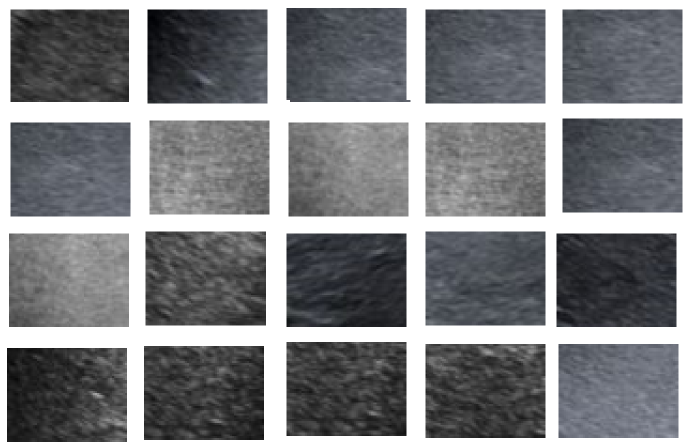

Figure 12: Homogeneous texture patches used to train the classifier for RoI detection of texture.

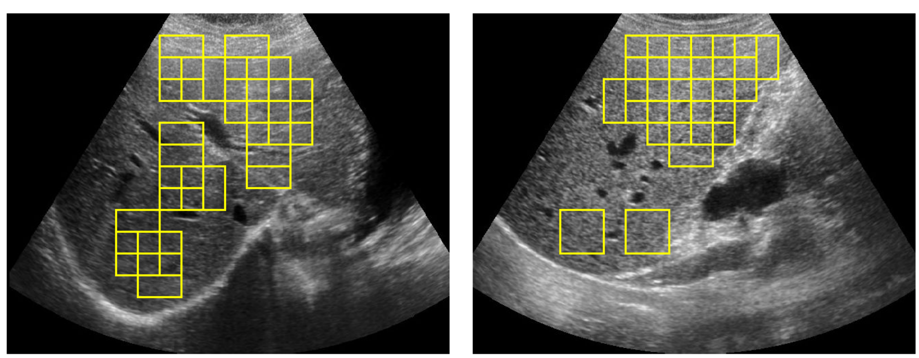

Figure 13: Performance of the proposed algorithm in detecting RoI for homogeneous patches. Yellow boxes indicates the RoI of homogeneous texture patterns corresponding to liver parenchyma.

quadratic, cubic and Gaussian kernels. The suitable kernels for the application is selected based on the experimental analysis. The inbuilt SVM function available in the MATLAB 2017a version is used in the experiment.

The optimal tuning parameters of different kernels are, for Cubic kernel: degree of polynomial=3, for Quadratic kernel: degree of polynomial=2, for Gaussian kernel: standard deviation=1. The kernel scale is set to '*auto*', data standardization is set to '*true*' with iterative single data algorithm as a solver.

3. Ultrasound data acquisition for analysis

The ultrasound database for the analysis is acquired by four sonographers all having more than 15 years of experience in performing ultrasound investigations. The ultrasound images are acquired using 3.5 MHz curved array transducer with clinical Seimens S1000 ultrasound scanning system. The ultrasound images are captured to a depth of 15 cm by adjusting the focal zone to the center of the organ for minimal beam diffraction. A total of 537 patients participated in the study, and they were in the age group of 18 to 55 years. All the patients were explained about the experiments in prior and taken a written consent form regarding the no objection in using their data for the study. A total of 537 liver ultrasound images along with 50 kidney image were used in the study. Only one image is acquired from a single patient. The images are acquired during the time period February 2017 to August 2017.

A total of 200 images were used in training process; these include 80 Normal, 45 Grade I, 40 Grade II and 35 Grade III images. The proposed algorithm is tested with two sets of the database, one consisting of 180 images which include 75 Normal, 60 Grade I and 45 Grade II images respectively, here Grade III images are not considered due to high obscuration of the RoI's. The second database consists 157 liver images. The images used in the first test case has not been used in the second test case. Performance of the proposed algorithm on the first database gives the overall accuracy of the algorithm in detecting the RoI's, while testing on the second database gives the performance of the algorithm on individual categories corresponding to different grades of fatty liver.

4. Experimental Analysis

4.1. Statistical analysis of the features

In this section, we present the statistical analysis of the features correspond to RoI's and nonRoI's used to train the classifier. The statistical analysis of the GIST features corresponding to diaphragm and periportal veins is shown in Table. 2. Since the size of GIST features is of 512, which is of high dimension, we presented the analysis only for the first 10 features. The mean for most of the GIST features corresponding to the TP's of the diaphragm is higher than that of the FP's resulted from the VJ algorithm and the standard deviation for the GIST features of FP's is observed to be low compared to the TP's of the VJ algorithm. For periportal veins, a clear distinction between the mean of the GIST features of TP's and FP's resulted from the VJ algorithm is observed. Similar to the diaphragm, the low standard deviation is observed in the GIST features of FP's compared to the TP's of the VJ algorithm. The similar trend is observed for rest of the GIST features. The mean and standard deviation of the histogram features extracted from homogeneous and nonhomogeneous regions is shown in Table. 3. The mean of histogram features for a homogeneous region is observed to be significantly lower than that of nonhomogenous histogram features and low standard deviation of the features is observed in histogram features of the homogeneous region compared to the nonhomogeneous region.

4.2. Performance analysis

In this section, we present the performance of the proposed algorithm for detecting each RoI. The VJ algorithm is trained by setting the following parameters: number of cascade classifiers=5, merge threshold=80, window enlargement in each step is set to 1.1 with sliding window shifted by one pixel.

Table 2: Mean and Standard deviation (Std) of the first ten GIST features of TP's and FP's of the diaphragm and periportal veins detected from VJ algorithm.

	RoI of Diaphragm				**RoI of periportal veins**			
	TP's		**FP's**		**TP's**		**FP's**	
No	**Mean**	**Std**	**Mean**	**Std**	**Mean**	**Std**	**Mean**	**Std**
1	0.0245	0.0074	0.0206	0.0001	0.0385	0.0156	0.0503	0.0007
2	0.0253	0.0062	0.0205	0.0002	0.0452	0.0221	0.0373	0.0002
3	0.0204	0.0066	0.0183	0.0003	0.0829	0.0360	0.0427	0.0004
4	0.0196	0.0048	0.0204	0.0002	0.0613	0.0322	0.0491	0.0006
5	0.0133	0.0032	0.0200	0.0001	0.1774	0.0695	0.0654	0.0014
6	0.0305	0.0075	0.0228	0.0002	0.0674	0.0337	0.0946	0.0011
7	0.0470	0.0106	0.0374	0.0001	0.1418	0.0661	0.0962	0.0031
8	0.0524	0.0124	0.0439	0.0004	0.0701	0.0272	0.0761	0.0015
9	0.0602	0.0372	0.0373	0.0002	0.0657	0.0213	0.0694	0.0018
10	0.0744	0.0199	0.0695	0.0002	0.0415	0.0222	0.0489	0.0006

Table 3: Mean and standard deviation of histogram features correspond to homogeneous and nonhomogeneous RoI.

	Homogeneous RoI		**Nonhomogeneous RoI**	
Features	**Mean**	**Std**	**Mean**	**Std**
Mean	0.2669	0.0478	0.3283	0.0659
variance	0.0079	0.0039	0.0340	0.0068
Skewness	0.6886	0.1938	1.2168	0.2566
Kurtosis	2.6839	0.7465	3.8265	0.7945

The VJ algorithm detects the RoI using sliding window approach due to which multiple detections will occur for each RoI. The multiple detections are eliminated by merging all the overlapped detections by taking an average for the coordinates of detected RoI's. Decreasing the merge threshold increased the number of FP's along with TP's and vice-versa. The optimal merge threshold of 80 is chosen based on the experimental analysis. The VJ algorithm used 7, 9, 11, 13 and 19 features at each stage of cascaded classifiers respectively. The performance of the proposed algorithm in detecting RoI for a diaphragm when VJ algorithm trained with different false alarm rates is shown in Table. 4. The algorithm is tested on 180 liver ultrasound images. The maximum classification accuracy of 97% is obtained at a false alarm rate of 0.5. Here the VJ algorithm detected the diaphragm with an accuracy of 98.2% with 450 FP's, after applying the GIST based cubic SVM classifier, FP's has been significantly reduced to 113.

The performance of the proposed algorithm in detecting the periportal veins is shown in Table. 5. The VJ algorithm used 7, 8, 10, 11 and 14 features in each cascaded stage respectively. The optimal trade-off between TP's and FP's is obtained at a merge threshold of 50. The proposed algorithm detected periportal veins with a maximum accuracy of 91% for the VJ algorithm when trained with a false alarm rate of 0.5. The VJ algortithm detected periportal veins with a maximum accuracy of 96% with 425 FP's. After applying GIST descriptor with quadratic SVM classifier, the number of FP's have significantly reduced to 43, which in turn also reduced the overall detection accuracy of periportal veins from 96% to 91%.

The histogram based Gaussian SVM classifier detected the RoI for homogeneous texture with 100% accuracy. The algorithm resulted with multiple RoI's for homogeneous textures along with FP's. The FP's are completely removed using the connected components algorithm.

Table 4: The accuracy of the proposed algorithm for detecting the RoI of a diaphragm.

False alarm rate	**Performance of Viola Jones algorithm**		**Performance of the algorithm after applying GIST descriptor + cubic SVM classifier**	
	Accuracy(%)	FP's	Accuracy(%)	FP's
0.1	91.0	160	85.0	14
0.2	93.5	194	87.4	21
0.3	94.7	260	89.7	44
0.4	96.0	390	96.0	78
0.5	98.2	450	97.0	113

Table 5: Accuracy of the proposed algorithm in detecting the periportal veins

False alarm rate	**Performance of Viola Jones algorithm**		**Performance of the algorithm after applying GIST descriptor + Quadratic SVM classifier**	
	Accuracy (%)	False Positive	Accuracy (%)	False Positive
0.1	89.7	84	84.0	9
0.2	91.7	131	87.0	15
0.3	93.0	141	89.6	16
0.4	94.9	314	90.7	25
0.5	96.0	425	91.0	43

Table 6: Accuracy of the proposed algorithm in detecting the RoI's with respect to different grades of fatty liver.

Category	Database	Diaphragm (%)	Periportal veins (%)
Normal	48	97.5	93.7
Grade I	33	95.5	92.3
Grade II	45	93.2	90.8
Grade III	31	65.7	80.3

4.3. Performance of the proposed algorithm with respect to different grades of fatty liver.

The performance of the proposed algorithm in detecting the RoI with respect to different grades of fatty liver is presented in this section. The liver ultrasound images correspond to different grades of fatty liver used in testing the proposed algorithm is shown in Fig. 14. The database consisted of 157 ultrasound images which include 48 normal, 33 Grade I, 45 Grade II and 31 Grade III images. For Normal, Grade I and Grade II images, the diaphragm and periportal veins are visible or partially visible to the normal eye. For 31 images of Grade III fatty liver, only for 15 images the diaphragm and periportal veins are partially visible, whereas for other images diaphragm and periportal veins are totally obscured and is not visible to the human eye. The accuracy of the proposed algorithm corresponding to different grades of the fatty liver is shown in Table. 6. The proposed algorithm detected diaphragm and periportal veins of the normal liver with an accuracy of 97.5% and 93.7% respectively. The accuracy of detecting diaphragm and periportal veins get reduced with an increase in the severity of the fat which resulted in obscuration of RoI. Even there is a high obscuration of RoI for Grade III fatty liver, the proposed algorithm detected diaphragm and periportal veins with an accuracy of 65.7% and 80.3% respectively. The classification accuracy is only computed for the images where diaphragms and periportal veins are perceivable to the human eye. For the images where diaphragm and periportal veins are not visible, the algorithm did not detect any RoI in the region with zero FP's. The proposed algorithm detected RoI for homogeneous patches with a 100% accuracy for all the liver ultrasound images. Since the organ boundaries are not visible in Grade III fatty liver ultrasound images, the RoI's detected outside the liver image is not recognizable. The brief remarks regarding the performance of the proposed algorithm in detecting each RoI is discussed in Table. 7. The result of the proposed algorithm in detecting the diaphragm, periportal veins and homogeneous texture of liver parenchyma is shown in Fig. 15.

The experiments are performed on a Windows desktop computer with Intel

Table 7: A brief summary regarding the performance of the proposed algorithm in detecting each RoI.

RoI detection	**Remarks**
Diaphragm	The bounding boxes enclosing some part of the diaphragm is detected using the VJ and GIST descriptor based cubic SVM classifier. The detected RoI is then used to initialize the active contour algorithm to detect the entire diaphragm. The bounding box position of RoI enclosing the diaphragm did not have an effect in detecting the entire contour of diaphragm since the active contour algorithm tends to capture the strong edges. The accuracy of detecting diaphragm decreased with increase in severity of fat in the liver due to obscuration of diaphragm.
Periportal veins	The bounding boxes enclosing periportal veins is detected using the VJ and GIST descriptor based quadratic SVM classifier. All the detected RoI's are completely enclosed within the RoI. The accuracy of detecting periportal veins decreased with increase in severity of fat in the liver due to obscuration of periportal veins.
Homogeneous texture	The RoI's are detected using the combination of histogram features based Gaussian SVM classifier and connected components algorithm. The algorithm resulted in multiple overlapping RoI's, and the end user can select an appropriate number of RoI's depending on the application. The accuracy of detecting RoI for homogeneous texture did not effected with the severity of fat present in the liver.

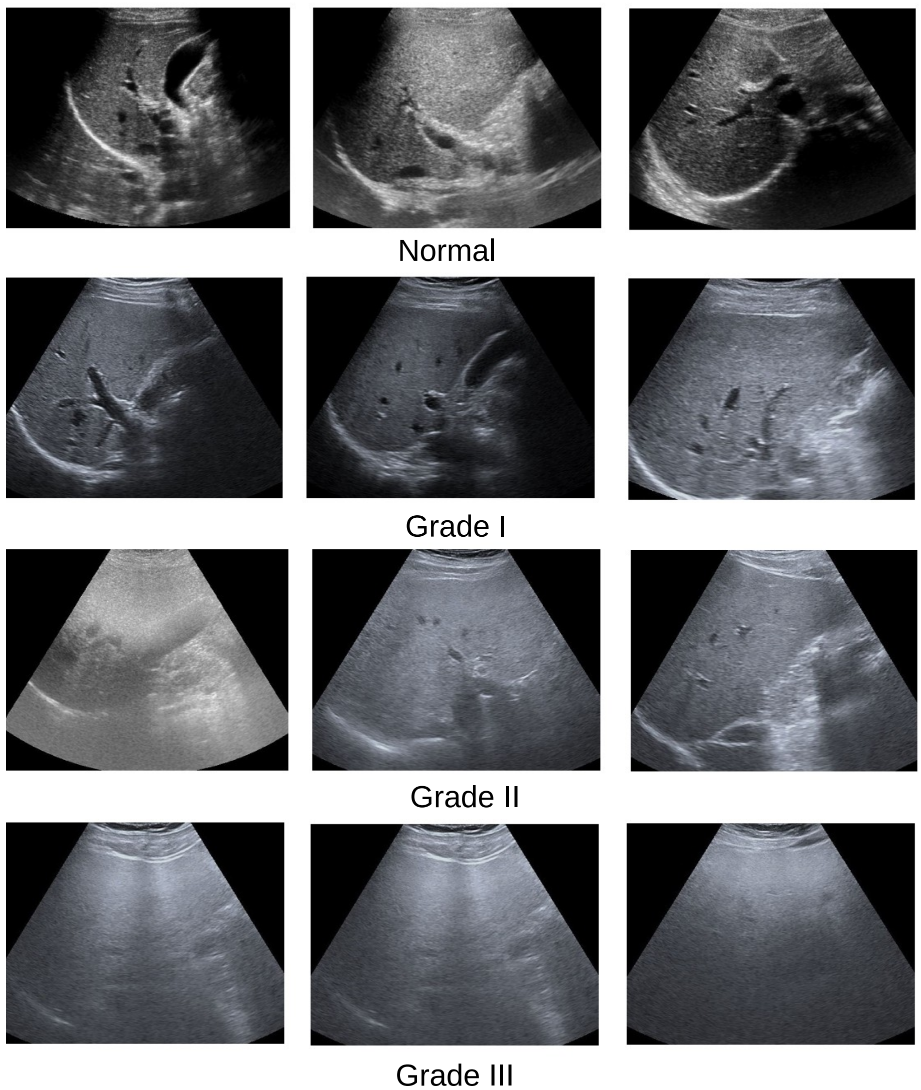

Figure 14: Images correspond to different grades of fatty liver. Images in each row belongs to single category.

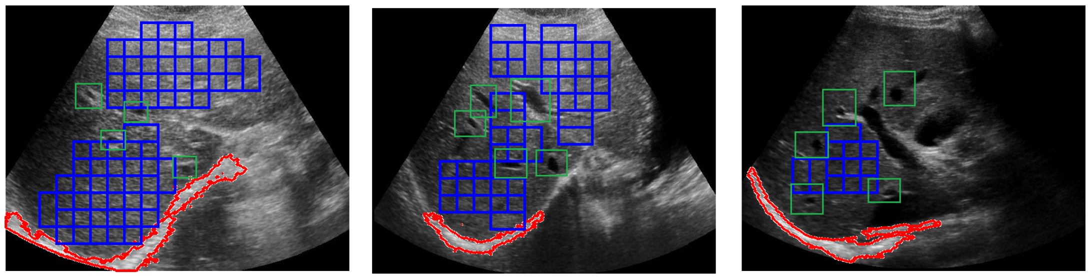

Figure 15: Performance of the proposed algorithm in detecting the RoI's. The region enclosed with red color represents the diaphragm, green boxes indicate the detection of periportal veins and blue boxes indicates the RoI of a homogeneous texture.

Core i7 processor, 16 GB RAM running with 2.8 GHz clock using MATLAB 2017a version. For an image of size 500×650, the algorithm took approximately 2.42 s for detecting RoI of a diaphragm, 2.5 s for segmenting the diaphragm after initialization, 4.3 s for periportal detection and 2.3 s for homogeneous texture detection. The algorithm took approximately 9 s for detecting multiple RoI's.

5. Discussion and conclusion

In this paper, we proposed a multi-model framework for automatic detection of diagnostically significant regions of fatty liver namely diaphragm, periportal veins and homogeneous texture in ultrasonic liver images. Since the characteristics of these regions vary with the fatty content of the liver, it poses a serious challenge in detecting these regions. The proposed algorithm detected the diaphragm, periportal veins and homogeneous texture of liver with an accuracy of 97%, 91% and 100% respectively. The accuracy of the proposed algorithm in detecting the RoI's in fatty liver decreased with increase in the severity of fat in the liver, this is justifiable since the visibility of diaphragm and periportal veins reduces with the severity of the disease. In literature, computer-aided algorithms developed for diagnosing the fatty liver involves manual intervention to crop the RoI's, hence making the algorithms semi-automated. The proposed algorithm eliminates the need for manual intervention by detecting the RoI's automatically, which can be used to develop accurate and automated diagnostic algorithms. The proposed algorithm benefits the sonographers to diagnose more number of patients by reducing the time needed to locate RoI's in the ultrasound image. As an extension of this work, we will work towards the development of automated algorithms for quantifying the fat in the liver based on detected RoI's.

References

[1] Takahashi, Yoshihisa, and Toshio Fukusato. Histopathology of nonalcoholic fatty liver disease/nonalcoholic steatohepatitis. World journal of gastroenterology: WJG 2014;20(42):15539.

[2] Bellentani, Stefano, Federica Scaglioni, Mariano Marino, and Giorgio Bedogni. Epidemiology of non-alcoholic fatty liver disease. Digestive diseases 2010;28(1):155-161.

[3] Marchesini, Giulio, Mara Brizi, Antonio M. Morselli-Labate, Giampaolo Bianchi, Elisabetta Bugianesi, Arthur J. McCullough, Gabriele Forlani, and Nazario Melchionda. Association of nonalcoholic fatty liver disease with insulin resistance." The American journal of medicine 1999; 107(5):450-455.

[4] Brunt, Elizabeth M., Christine G. Janney, Adrian M. Di Bisceglie, Brent A. Neuschwander-Tetri, and Bruce R. Bacon. Nonalcoholic steatohepatitis: a proposal for grading and staging the histological lesions. The American journal of gastroenterology 1999; 94(9):2467-2474.

[5] Lee, Seung Soo, and Seong Ho Park. Radiologic evaluation of nonalcoholic fatty liver disease. World journal of gastroenterology: WJG 2014;20(23):7392.

[6] Goceri, Evgin, Zarine K. Shah, Rick Layman, Xia Jiang, and Metin N. Gurcan. Quantification of liver fat: A comprehensive review. Computers in biology and medicine 2016;71:174-189

[7] Hernaez, Ruben, Mariana Lazo, Susanne Bonekamp, Ihab Kamel, Frederick L. Brancati, Eliseo Guallar, and Jeanne M. Clark. Diagnostic accuracy and reliability of ultrasonography for the detection of fatty liver: A metaanalysis. Hepatology 2011; 54(3):1082-1090.

[8] Allan, Richard, Kerry Thoirs, and Maureen Phillips. Accuracy of ultrasound to identify chronic liver disease. World Journal of Gastroenterology: WJG 2010;16(28):3510.

[9] Strauss, S., Gavish, E., Gottlieb, P., & Katsnelson, L.Interobserver and intraobserver variability in the sonographic assessment of fatty liver. American Journal of Roentgenology 2007;189(6):320-323.

[10] Bharti, Puja, Deepti Mittal, and Rupa Ananthasivan. Computer-aided Characterization and Diagnosis of Diffuse Liver Diseases Based on Ultrsound Imaging: A Review. Ultrasonic imaging 2017;39(1):33-61.

[11] Alivar, Alaleh, Habibollah Danyali, and Mohammad Sadegh Helfroush. Hierarchical classification of normal, fatty and heterogeneous liver diseases from ultrasound images using serial and parallel feature fusion." Biocybernetics and Biomedical Engineering 2016;36(4):697-707.

[12] Biswas, Mainak, Venkatanareshbabu Kuppili, Damodar Reddy Edla, Harman S. Suri, Luca Saba, Rui Tato Marinhoe, J. Miguel Sanches, and Jasjit S.Suri. Symtosis: A liver ultrasound tissue characterization and risk stratification in optimized deep learning paradigm. Computer methods and programs in biomedicine 2018;155:165-177.

[13] Badawi, Ahmed M., Ahmed S. Derbala, and Abou-Bakr M. Youssef. Fuzzy logic algorithm for quantitative tissue characterization of diffuse liver diseases from ultrasound images. International Journal of Medical Informatics 1999; 55(2):135-147.

[14] Kyriacou, E., Pavlopoulos, S., Konnis, G., Koutsouris, D., Zoumpoulis, P. and Theotokas, L.r. Computer assisted characterization of diffused liver

disease using image texture analysis techniques on B-scan images. In Nuclear Science Symposium IEEE 1997;(2):1479-1483.

[15] Acharya, U. Rajendra, S. Vinitha Sree, Ricardo Ribeiro, Ganapathy Krishnamurthi, Rui Tato Marinho, Joo Sanches, and Jasjit S. Suri. Data mining framework for fatty liver disease classification in ultrasound: a hybrid feature extraction paradigm. Medical physics 2012;39(7Part1): 4255-4264.

[16] Pavlopoulos, S., E. Kyriacou, D. Koutsouris, K. Blekas, A. Stafylopatis, and P. Zoumpoulis. Fuzzy neural network-based texture analysis of ultrasonic images. IEEE Engineering in Medicine and Biology Magazine 2000;19(1):39-47.

[17] Acharya, U. Rajendra, Joel En Wei Koh, Yuki Hagiwara, Jen Hong Tan, Arkadiusz Gertych, Anushya Vijayananthan, Nur Adura Yaakup, Basri Johan Jeet Abdullah, Mohd Kamil Bin Mohd Fabell, and Chai Hong Yeong. Automated diagnosis of focal liver lesions using bidirectional empirical mode decomposition features. Computers in Biology and Medicine 2018.

[18] Wu, Cheng-Chi, Wen-Li Lee, Yung-Chang Chen, and Kai-Sheng Hsieh. Evolution-based hierarchical feature fusion for ultrasonic liver tissue characterization. IEEE journal of biomedical and health informatics 2013; 17(5):967-976.

[19] Singh, Mandeep, Sukhwinder Singh, and Savita Gupta. An information fusion based method for liver classification using texture analysis of ultrasound images." Information Fusion 2014;19:91-96.

[20] Liao, Yin-Yin, Kuen-Cheh Yang, Ming-Ju Lee, Kuo-Chin Huang, Jin-De Chen, and Chih-Kuang Yeh. Multifeature analysis of an ultrasound quantitative diagnostic index for classifying nonalcoholic fatty liver disease. Scientific reports 2016;6.

[21] L. Laura, W. Rachel, T. Emmanuel. Metabolic and cardiovascular complications in the liver transplant recipient," Ann . Gastroenterol 2015;28:111.

[22] V. Khullar, A. Dolganiuc, R. J. Firpi. Pre-and-post transplant considerations in patients with nonalcoholic fatty liver disease. World J.Transpl. 2014;4(2):8192.

[23] Bharath, R., Pradeep Kumar Mishra, and P. Rajalakshmi. Automated quantification of ultrasonic fatty liver texture based on curvelet transform and SVD." Biocybernetics and Biomedical Engineering 2017.

[24] R. Bharath and P. Rajalakshmi. Deep scattering convolution network based features for ultrasonic fatty liver tissue characterization. In Engineering in Medicine and Biology Society (EMBC), 39th Annual International Conference of the IEEE 2017;1982-1985.

[25] Lupsor, M., R. Badea, C. Vica, S. Nedevschi, M. Grigorescu, C. Radu, H. Stefanescu, and D. Crisan. Non-invasive steatosis assessment in NASH through the computerized processing of ultrasound images: Attenuation versus textural parameters. In Automation Quality and Testing Robotics (AQTR), IEEE International Conference on 2010;2:1-6.

[26] Ier, Semra, Abdulhakim Cokun, and Trkan kizceli. Quantitative grading using grey relational analysis on ultrasonographic images of a fatty liver. Journal of medical systems 2012;36(4):2521-2528.

[27] Mihailescu, Dan Mihai, Vasile Gui, Corneliu Ioan Toma, Alina Popescu, and Ioan Sporea. Automatic evaluation of steatosis by ultrasound image analysis. In Electronics and Telecommunications (ISETC), 10th International Symposium on, IEEE, 2012:311-314.

[28] Vicas, Cristian, Sergiu Nedevschi, Monica Lupsor, and Radu Badea. Automatic detection of liver capsule using Gabor filters. Applications in steatosis quantification. In Intelligent Computer Communication and Processing, IEEE 5th International Conference on, IEEE, 2009:133-140.

[29] Acharya, U. Rajendra, Hamido Fujita, Shreya Bhat, U. Raghavendra, Anjan Gudigar, Filippo Molinari, Anushya Vijayananthan, and Kwan Hoong

Ng. Decision support system for fatty liver disease using GIST descriptors extracted from ultrasound images. Information Fusion 2016;29:32-39.

[30] Acharya, U. Rajendra, U. Raghavendra, Hamido Fujita, Yuki Hagiwara,Joel EW Koh, Tan Jen Hong, Vidya K. Sudarshan et al. Automated characterization of fatty liver disease and cirrhosis using curvelet transform and entropy features extracted from ultrasound images. Computers in biology and medicine 2016;79:250-258.

[31] Acharya, U. Rajendra, Oliver Faust, Filippo Molinari, S. Vinitha Sree, Sameer P. Junnarkar, and Vidya Sudarshan. Ultrasound-based tissue characterization and classification of fatty liver disease: A screening and diagnostic paradigm. Knowledge-Based Systems 2015;75:66-77.

[32] Acharya, U.R., Fujita, H., Sudarshan, V.K., Mookiah, M.R.K., Koh, J.E.,Tan, J.H., Hagiwara, Y., Chua, C.K., Junnarkar, S.P., Vijayananthan, A. and Ng, K.H. An integrated index for identification of fatty liver disease using radon transform and discrete cosine transform features in ultrasound images. Information Fusion 2016;31:43-53.

[33] Singh, Divya, Chandan J. Das, and Manas P. Baruah. Imaging of non alcoholic fatty liver disease: A road less travelled. Indian journal of endocrinology and metabolism 2013;17(6):990.

[34] Viola, Paul, and Michael J. Jones. Robust real-time face detection. International journal of computer vision 2004; 57(2):137-154.

[35] Oliva, Aude, and Antonio Torralba. Modeling the shape of the scene: A holistic representation of the spatial envelope. International journal of computer vision 2001;42(3):145-175.

[36] Chan, Tony F., and Luminita A. Vese. Active contours without edges. IEEE Transactions on image processing 2001:10(2):266-277

[37] Kass, Michael, Andrew Witkin, and Demetri Terzopoulos. Snakes: Active contour models. International journal of computer vision 1988; 1(4):321-331.

[38] Haralock, Robert M., and Linda G. Shapiro. Computer and robot vision. Addison-Wesley Longman Publishing Co., Inc., 1991.

[39] Sarwal, Aarti, Francis O. Walker, and Michael S. Cartwright. Neuromuscular ultrasound for evaluation of the diaphragm. Muscle & nerve 2013; 47(3):319-329.

[40] Chu C, Bai J, Liu L, Wu X, Zheng G. Fully automatic segmentation of hip CT images via random forest regression-based Atlas selection and optimal graph search-based surface detection. In Asian Conference on Computer Vision Springer, Cham 2014;1:640-654.

[41] Bharath, R., Punit Kumar, Chandrashekar Dusa, Vivek Akkala, Suresh Puli, Harsha Ponduri, K. Divya Krishna et al. FPGA-Based Portable Ultrasound Scanning System with Automatic Kidney Detection. Journal of Imaging 2015; 1(1):193-219.

[42] Bharath, R., Pallavi Vaish, and P. Rajalakshmi. Implementation of diagnostically driven compression algorithms via WebRTC for IoT enabled tele-sonography. In Biomedical Engineering and Sciences (IECBES), IEEE EMBS Conference on, IEEE 2016:204-209.

[43] ha K, Maek J, Burget R, Bene R, Zvodn E. Novel method for localization of common carotid artery transverse section in ultrasound images using modified Viola-Jones detector. Ultrasound in medicine & biology 2013;39(10):1887-902.

[44] Wang, Yi-Qing. An analysis of the Viola-Jones face detection algorithm. Image Processing On Line 2014;4:128-148.

[45] Simard, Patrice, Lon Bottou, Patrick Haffner, and Yann LeCun. Boxlets: a fast convolution algorithm for signal processing and neural networks. In Advances in Neural Information Processing Systems 1999; 571-577.

[46] Freund, Yoav, and Robert E. Schapire. A desicion-theoretic generalization of on-line learning and an application to boosting. In European conference on computational learning theory, Springer, Berlin, Heidelberg, 1995:23-37.

[47] Dalal, Navneet, and Bill Triggs. Histograms of oriented gradients for human detection. In Computer Vision and Pattern Recognition, CVPR 2005. IEEE Computer Society Conference on 2005;1:886-893.

[48] Douze M, Jgou H, Sandhawalia H, Amsaleg L, Schmid C. Evaluation of gist descriptors for web-scale image search. In Proceedings of the ACM International Conference on Image and Video Retrieval 2009:19

[49] Oliva A. Gist of the scene. Neurobiology of attention. 2005;696(64):251-8.

[50] Cootes, Timothy F., Andrew Hill, Christopher J. Taylor, and Jane Haslam. Use of active shape models for locating structures in medical images. Image and vision computing 1994;12(6):355-365.

[51] Xu, Chenyang, and Jerry L. Prince. Snakes, shapes, and gradient vector flow. IEEE Transactions on image processing 1998;7(3):359-369.

[52] Cohen, Laurent D. On active contour models and balloons. CVGIP: Image understanding 1991; 53(2):211-218.

[53] 53. Cremers, Daniel, Christoph Schnorr, and Joachim Weickert. Diffusion snakes: combining statistical shape knowledge and image information in a variational framework. In Variational and Level Set Methods in Computer Vision, 2001. Proceedings. IEEE Workshop on;137-144.

[54] Caselles, Vicent, Ron Kimmel, and Guillermo Sapiro. Geodesic active contours. International journal of computer vision 1997;22(1): 61-79.

[55] Chang, Chih-Chung, and Chih-Jen Lin. LIBSVM: a library for support vector machines. ACM transactions on intelligent systems and technology (TIST) 2011;2(3):27.

[56] Schlkopf, Bernhard, and Alexander J. Smola. Learning with kernels: support vector machines, regularization, optimization, and beyond. MIT press, 2002.